

Strengthening the Magnetic Interactions in Pseudobinary First-Row Transition Metal Thiocyanates, $M(\text{NCS})_2$

Euan N. Bassey, Joseph A. M. Paddison, Evan N. Keyzer, Jeongjae Lee, Pascal Manuel, Ivan da Silva, Siân E. Dutton, Clare P. Grey,* and Matthew J. Cliffe*

Cite This: <https://dx.doi.org/10.1021/acs.inorgchem.0c01478>

Read Online

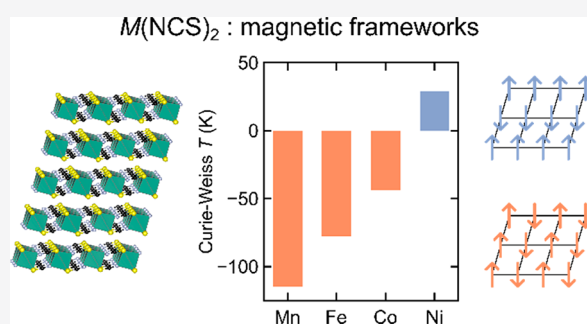
ACCESS |

Metrics & More

Article Recommendations

Supporting Information

ABSTRACT: Understanding the effect of chemical composition on the strength of magnetic interactions is key to the design of magnets with high operating temperatures. The magnetic divalent first-row transition metal (TM) thiocyanates are a class of chemically simple layered molecular frameworks. Here, we report two new members of the family, manganese(II) thiocyanate, $\text{Mn}(\text{NCS})_2$, and iron(II) thiocyanate, $\text{Fe}(\text{NCS})_2$. Using magnetic susceptibility measurements on these materials and on cobalt(II) thiocyanate and nickel(II) thiocyanate, $\text{Co}(\text{NCS})_2$ and $\text{Ni}(\text{NCS})_2$, respectively, we identify significantly stronger net antiferromagnetic interactions between the earlier TM ions—a decrease in the Weiss constant, θ , from 29 K for $\text{Ni}(\text{NCS})_2$ to -115 K for $\text{Mn}(\text{NCS})_2$ —a consequence of more diffuse 3d orbitals, increased orbital overlap, and increasing numbers of unpaired t_{2g} electrons. We elucidate the magnetic structures of these materials: $\text{Mn}(\text{NCS})_2$, $\text{Fe}(\text{NCS})_2$, and $\text{Co}(\text{NCS})_2$ order into the same antiferromagnetic commensurate ground state, while $\text{Ni}(\text{NCS})_2$ adopts a ground state structure consisting of ferromagnetically ordered layers stacked antiferromagnetically. We show that significantly stronger exchange interactions can be realized in these thiocyanate frameworks by using earlier TMs.



1. INTRODUCTION

The rational design and synthesis of new magnetic materials tailored to particular functions requires an understanding of the fundamental interactions taking place between magnetic centers. Magnetic molecular framework materials—that is, systems in which magnetic centers are connected via molecular ligands into lattices—present an excellent opportunity to study these interactions and their chemical origins.

Using molecular bridging ligands to connect paramagnetic metal centers can produce open and flexible structures, permitting potential applications such as multiferroics,^{1–3} magnetostrictive materials,⁴ and magnetic sensors.^{5–7} The properties of molecular frameworks are not determined by long-range electrostatic forces—as in oxide frameworks—but are instead dominated by short-range coordination bonds between the metal center, M, and its ligands, L.⁸ The nature and delocalization of the M–L bond control the exchange interactions and therefore the magnetic properties of the material. By careful choice of L, very anisotropic structures can be created, which may have low-dimensional magnetic properties.^{9–15}

Low-dimensional magnetic materials are an example of many-body quantum systems amenable to exact mathematical treatment.¹⁶ In particular, the study of the behavior of low-dimensional magnets is of critical importance to spin-liquids^{17,18} and high-temperature superconductivity.¹⁹

Thiocyanate, $(\text{NCS})^-$, is a promising ligand in magnetic molecular frameworks, as it is capable of promoting strong superexchange interactions between paramagnetic metal centers—for example, $J = +230$ K in $\text{Cu}_2(\text{NCS})_4(\text{bpm})$ ($\text{bpm} = 2,2$ -bipyrimidine).^{9,20–25} However, the majority of the frameworks studied thus far incorporate ancillary ligands, which can decrease metal–metal connectivity in the framework and thereby the net strength of interactions (as measured by the Weiss constant, θ).^{20,21}

Despite the range of complex magnetic thiocyanate compounds reported,²⁶ the parent pseudobinary system, $M(\text{NCS})_2$, is relatively unexplored, with only three known magnetic examples: $\text{Co}(\text{NCS})_2$,²⁰ $\text{Ni}(\text{NCS})_2$,^{27,28} and $\text{Cu}(\text{NCS})_2$.⁹ $\text{Cu}(\text{NCS})_2$ is a quasi-one-dimensional magnet, due to the Jahn–Teller distortion of the Cu^{2+} ions, with strong superexchange interactions along the $\text{Cu}(\text{NCS})_2$ chain ($J = 133$ K), but a significantly lower Néel temperature, $T_N = 12$ K.⁹

Previous work has established that both $\text{Co}(\text{NCS})_2$ ²⁰ and $\text{Ni}(\text{NCS})_2$ ²⁸ order antiferromagnetically, with $T_N = 22$ and 52

Received: May 20, 2020

K, respectively. However, the value of θ for $\text{Ni}(\text{NCS})_2$ suggested net ferromagnetic interactions ($\theta = 39.8$ K);²⁸ in contrast, $\text{Co}(\text{NCS})_2$ has net antiferromagnetic interactions ($\theta = -40$ K).²⁰ At present, the magnetic structures of $\text{Co}(\text{NCS})_2$ and $\text{Ni}(\text{NCS})_2$ are unknown, which makes rationalizing the differences in the values of θ challenging.

The structures adopted by $\text{M}(\text{NCS})_2$ are directly analogous to the corresponding transition metal (TM) halides, MX_2 [Figure 1]. MX_2 consists of layers of edge-sharing M^{2+}

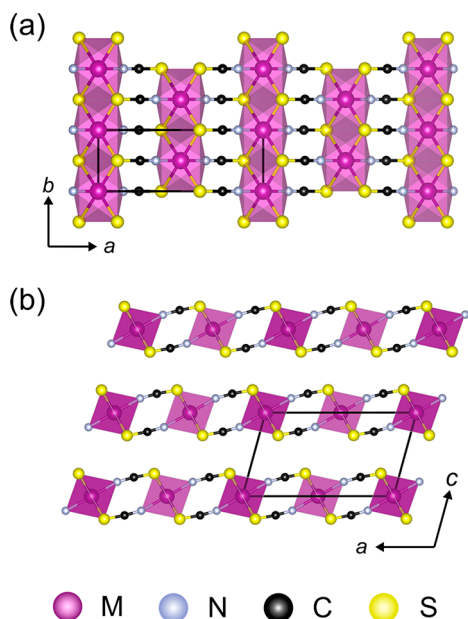


Figure 1. (a) Projection of a $(2 \times 2 \times 1)$ supercell of $\text{M}(\text{NCS})_2$ ($\text{M} = \text{Mn}, \text{Fe}, \text{Co}, \text{Ni}$) down the c axis, highlighting the layers of edge-sharing $[\text{M}^{2+}\text{N}_2\text{S}_4]$ octahedra. (b) Projection of a $(2 \times 1 \times 2)$ supercell of $\text{M}(\text{NCS})_2$ down the b axis, showing the stacking of layers.

octahedra with weak van der Waals interactions between the layers [Figure 1].^{20,27} The triangular metal sublattice lends itself to geometric frustration^{29–31} and hence leads to unusual magnetic properties, such as multiferroic behavior and helimagnetism.^{32–36} Furthermore, the strength of magnetic interactions in MX_2 is comparable to those in $\text{M}(\text{NCS})_2$, for example, $\text{Ni}(\text{NCS})_2$ ($T_N = 52$ K)²⁸ and NiBr_2 ($T_N = 44$ K).^{32,37}

In $\text{M}(\text{NCS})_2$ ($\text{M} = \text{Co}, \text{Ni}$), the metal sites form layers of an anisotropic triangular lattice, and so $\text{M}(\text{NCS})_2$ has the potential to show similar unusual magnetic behavior. The two nearest-neighbor interactions within the layers are J_1 , along the $\text{M}-\text{S}-\text{M}$ chains (along the $[010]$ direction), and J_2 , through $\text{M}-\text{NCS}-\text{M}$ linkages [Figure 2b and c]; the Heisenberg Hamiltonian for this system may be written as

$$\hat{H} = \sum_{i,j} S_i J_{ij} S_j \quad (1)$$

where the summation is taken over all nearest-neighbor pairs of spins i and j with a Heisenberg exchange constant J_{ij} between them. Here, each pair is counted once, and positive values of J_{ij} correspond to antiferromagnetic interactions. In $\text{Cu}(\text{NCS})_2$, just as in CuCl_2 and CuBr_2 , ordering of the Jahn–Teller distortion lowers the structural symmetry and disrupts the superexchange pathways, producing quasi one-dimensional magnetism.^{9,38,39}

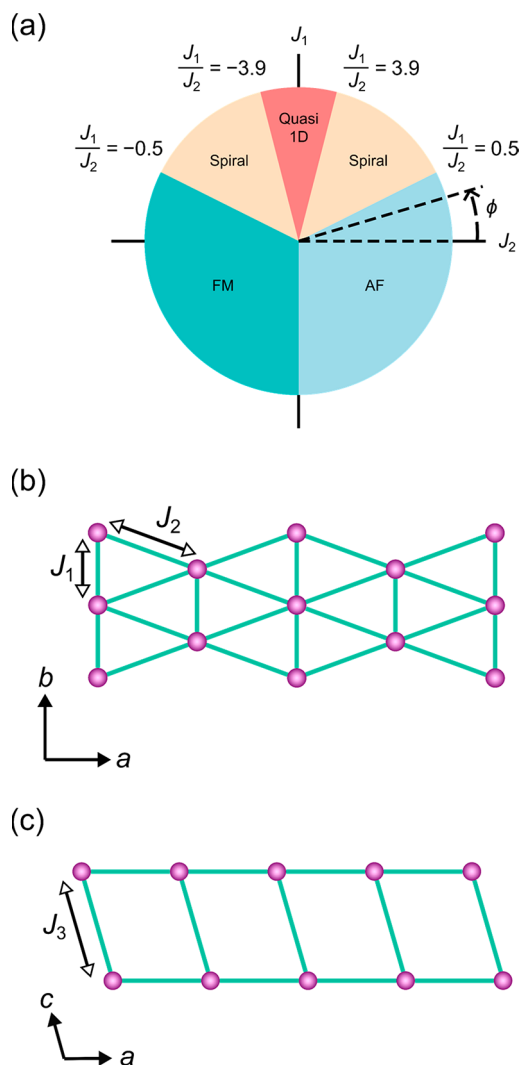


Figure 2. (a) Classical Heisenberg magnetic phase diagram for an anisotropic two-dimensional triangular lattice, adapted from ref 41. The nearest-neighbor exchange interactions, J_1 and J_2 , are illustrated in b, while the interlayer coupling constant, J_3 , is illustrated in c.

The spatially anisotropic triangular lattice may be characterized using a single parameter, $\phi = \tan^{-1}(J_1/J_2)$ [Figure 2a].^{40,41} By varying J_1 and J_2 , the isotropic triangular lattice ($J_1 = J_2$, $\phi = \pi/4$) can be transformed into a square lattice ($J_1 = 0$, $\phi = 0, \pi$) or a quasi-one-dimensional chain ($J_2 = 0$, $\phi = \pi/2$). Although we anticipate the presence of a small finite interlayer coupling, perhaps mediated via $\text{S}\cdots\text{S}$ interlayer contacts⁴² (J_3 , where we expect $J_3 \ll J_1, J_2$), this two-dimensional phase diagram will still provide a qualitative reference for the observed phases, as has been found for other van der Waals magnets with comparable interlayer distances.^{32–35,41,43–45}

In this work, we synthesized and characterized $\text{M}(\text{NCS})_2$ ($\text{M} = \text{Mn}, \text{Fe}, \text{Co}$ and Ni)— $\text{M} = \text{Mn}$ and Fe for the first time. The materials were characterized using powder X-ray diffraction, thermogravimetric analysis, and diffuse reflectance spectroscopy. In addition, we measured their magnetic properties using magnetic susceptibility measurements and powder neutron diffraction (PND) and determined constraints on the relative sizes of their magnetic exchange interactions.

We show that the net strength of superexchange interactions, as measured by the Weiss constant, θ , increases

and becomes increasingly antiferromagnetic as we move to earlier first-row TM cations.

From PND measurements, $\text{Mn}(\text{NCS})_2$, $\text{Fe}(\text{NCS})_2$, and $\text{Co}(\text{NCS})_2$ are observed to adopt the same commensurate stripe-ordered magnetic ground state with ordering vector $\mathbf{k} = [100]^*$. In contrast, $\text{Ni}(\text{NCS})_2$ adopts a ground state magnetic structure with ordering vector $\mathbf{k} = [00\frac{1}{2}]^*$, consistent with its very different (and positive) Weiss constant.

2. MATERIALS AND METHODS

2.1. Synthesis. The synthetic procedures for each member of the $\text{M}(\text{NCS})_2$ ($\text{M} = \text{Mn}, \text{Fe}, \text{Co},$ and Ni) used were broadly similar. We therefore provide a general synthetic route for $\text{M}(\text{NCS})_2$ here; complete synthetic routes for each compound are given in the Supporting Information.

For $\text{M} = \text{Mn}, \text{Co},$ and Ni , TM sulfate salts were dissolved in the minimum volume of deionized H_2O and added to a saturated solution of $\text{Ba}(\text{SCN})_2 \cdot 3\text{H}_2\text{O}$. For $\text{M} = \text{Fe}$, a solution of KSCN in dry acetonitrile was added to $\text{Fe}(\text{BF}_4)_2 \cdot 6\text{H}_2\text{O}$. In all cases, a white precipitate (colored by the strongly colored solution) formed immediately, and the reaction mixture was stirred in the air ($\text{M} = \text{Mn}, \text{Co},$ and Ni) or under a nitrogen atmosphere ($\text{M} = \text{Fe}$). The solvent was then removed *in vacuo* to generate a microcrystalline powder.

2.2. Powder X-ray Diffraction (PXRD). Phase purity was assessed via powder diffraction measurements on a PANalytical Empyrean Diffractometer using $\text{Cu K}\alpha$ radiation ($\lambda = 1.541 \text{ \AA}$) in Bragg–Brentano geometry. Diffraction patterns were recorded over the range $2\theta = 5\text{--}80^\circ$ using a step size of 0.02° and a scan speed of $0.01^\circ \text{ s}^{-1}$. Due to their sensitivity to moisture and air, the diffraction patterns of $\text{Mn}(\text{NCS})_2$ and $\text{Fe}(\text{NCS})_2$ were measured by encasing the samples between polyimide (Kapton) films. All diffraction patterns were analyzed via Pawley⁴⁶ and Rietveld^{47,48} refinements using TOPAS Academic 6 structure refinement software.^{49,50}

2.3. Diffuse Reflectance Spectroscopy. Diffuse reflectance spectra were recorded on an Agilent Technologies UV–vis spectrometer, connected via optical fiber to a Cary 50 Diffuse Reflectance Accessory, using a wavelength range $\lambda = 200\text{--}1000 \text{ nm}$, with a step size of 1.00 nm and scan rate of 10 nm s^{-1} . In all cases, samples were diluted with BaSO_4 powder—either in a 1:10 mass ratio ($\text{Fe}(\text{NCS})_2$, $\text{Co}(\text{NCS})_2$, and $\text{Ni}(\text{NCS})_2$) or a 1:1 mass ratio ($\text{Mn}(\text{NCS})_2$)—and the mixture was ground to produce a homogeneous powder, which was then loaded between two quartz discs. For $\text{Mn}(\text{NCS})_2$ and $\text{Fe}(\text{NCS})_2$, the homogeneous powders were prepared inside an Ar-filled glovebox and the quartz discs sealed with Parafilm; the spectra for these compounds were acquired within half an hour of removing the samples and discs from the glovebox.

For all materials, the spectra were averaged over multiple measurements; spikes in the average due to erroneous spikes in the raw data—i.e., spikes in one spectrum which do not repeat in the other spectra, likely due to specular reflection from the powder—were removed from the average and the “spiked” data point replaced with the average intensity either side of the spike.

2.4. Thermogravimetric Analysis (TGA). Thermogravimetric data for each compound were recorded with a Mettler-Toledo Thermogravimetric Analysis/Simultaneous Differential Thermal Analysis (TGA/SDTA) 851 Thermobalance. Each powder sample (20–50 mg) was loaded into an alumina crucible and heated from 50 to 600°C at a heating rate of $10^\circ \text{C min}^{-1}$ under a nitrogen atmosphere. The data collected were measured relative to a background blank TGA curve, recorded using the same alumina crucible, temperature range, and heating rate, under a nitrogen atmosphere.

2.5. Magnetic Susceptibility Measurements. The magnetic susceptibility measurements were carried out on powder samples (10–20 mg) using a Quantum Design Magnetic Property Measurement System 3 (MPMS) superconducting quantum interference device (SQUID) magnetometer. The zero-field cooled (ZFC) and

field-cooled (FC) susceptibilities were measured in a field of 0.01 T over a temperature range of $2\text{--}300 \text{ K}$. As $M(H)$ is linear in this field range, the small-field approximation to the susceptibility, $\chi \approx M/H$, was assumed to be valid. The data for each compound were corrected for diamagnetism of the sample using Pascal's constants.⁵¹

2.6. Powder Neutron Diffraction (PND). Powder neutron diffraction measurements were carried out at the ISIS Pulsed Neutron and Muon Source using the WISH ($\text{Mn}(\text{NCS})_2$, $\text{Co}(\text{NCS})_2$, $\text{Ni}(\text{NCS})_2$) and GEM ($\text{Fe}(\text{NCS})_2$) instruments.⁵² Samples of $\text{Mn}(\text{NCS})_2$ (4.76 g), $\text{Fe}(\text{NCS})_2$ (2.26 g), $\text{Co}(\text{NCS})_2$ (2.44 g), and $\text{Ni}(\text{NCS})_2$ (4.76 g) were loaded into thin-walled vanadium canisters. The canister diameters were 11 mm for $\text{Mn}(\text{NCS})_2$ and $\text{Ni}(\text{NCS})_2$, 6 mm for $\text{Co}(\text{NCS})_2$, and 6 mm with an indium seal for $\text{Fe}(\text{NCS})_2$. Each sample was loaded to a height of at least 40 mm , to ensure the full beam illuminates the sample.

Each sample was first cooled to the base temperature (1.5 K for $\text{Mn}(\text{NCS})_2$, $\text{Co}(\text{NCS})_2$, and $\text{Ni}(\text{NCS})_2$ and 10 K for $\text{Fe}(\text{NCS})_2$), and diffraction patterns were then collected at a series of temperatures through T_N . A complete list of temperature steps and data collections may be found in the Supporting Information. The data were corrected for absorption effects using the Mantid software package.⁵³

For each compound, the nuclear structure was determined by Rietveld refinement against powder neutron diffraction data collected above T_N , using a model derived from the previously reported single crystal structure of $\text{Ni}(\text{NCS})_2$.²⁷ All refinements were carried out using TOPAS Academic 6.0.⁵⁰

Rietveld refinements using the candidate magnetic irreducible representations (irreps) were carried out for each compound separately, which showed that in each case only one of the two single irrep structures was consistent with the experimental data. Including the second irrep did not significantly improve the fit to the data. On this basis, we refined the magnetic structures using only the mY_2^+ irrep for $\text{Mn}(\text{NCS})_2$, $\text{Co}(\text{NCS})_2$, and $\text{Fe}(\text{NCS})_2$ and the mA_1^+ irrep for $\text{Ni}(\text{NCS})_2$. All refinements were carried out by simultaneously refining against data collected on multiple banks of detectors: on WISH, for $\text{Mn}(\text{NCS})_2$, banks 2–5; for $\text{Co}(\text{NCS})_2$, banks 1–5; and for $\text{Ni}(\text{NCS})_2$, banks 2–5; on GEM, for $\text{Fe}(\text{NCS})_2$, banks 2–5.

In all cases, the background was fit with a 12-term Chebyshev polynomial. For the final refinements of the data collected for $\text{Mn}(\text{NCS})_2$ using the WISH diffractometer and for the final refinement of the data collected for $\text{Fe}(\text{NCS})_2$ on the GEM diffractometer, it proved necessary to refine the Voigt peak-shape parameters separately for high Q and low Q data, due to their unusual Q dependence.

For all refinements, the lattice parameters, atomic positions, and magnitudes and directions of the magnetic moments were allowed to refine freely, aside from restraints on the C–N (ca. 1.15 \AA) and C–S (ca. 1.65 \AA) bond lengths. For $\text{Mn}(\text{NCS})_2$, $\text{Co}(\text{NCS})_2$, and $\text{Ni}(\text{NCS})_2$, the same set of freely refining anisotropic atomic displacement parameters was used for each atom, while the same isotropic atomic displacement parameter was refined for each atom in $\text{Fe}(\text{NCS})_2$ [Table S6]. The bond lengths and angles were consistent with those expected from previous studies [Table S1].^{20,27}

3. RESULTS

3.1. Bulk Characterization. The $\text{M}(\text{NCS})_2$ family members ($\text{M} = \text{Mn}^{2+}, \text{Fe}^{2+}, \text{Co}^{2+}, \text{Ni}^{2+}$) were synthesized via salt metathesis reactions, driven by precipitation of an insoluble side-product (BaSO_4 for $\text{M} = \text{Mn}, \text{Co}, \text{Ni}$; KBF_4 for $\text{M} = \text{Fe}$). Apart from $\text{Ni}(\text{NCS})_2$, all compounds crystallized as solvates; the cocrystallized solvent was removed by heating either *in vacuo* ($\text{M} = \text{Fe}, \text{Mn}$) or in the air ($\text{M} = \text{Co}$). While $\text{Co}(\text{NCS})_2$ and $\text{Ni}(\text{NCS})_2$ were stable in the air, $\text{Mn}(\text{NCS})_2$ and $\text{Fe}(\text{NCS})_2$ were moisture- and air-sensitive, respectively. The phase purity of all materials was checked initially using PXRD [Figure S1], revealing the presence of trace quantities (<1 wt %) of impurities such as unreacted starting materials or

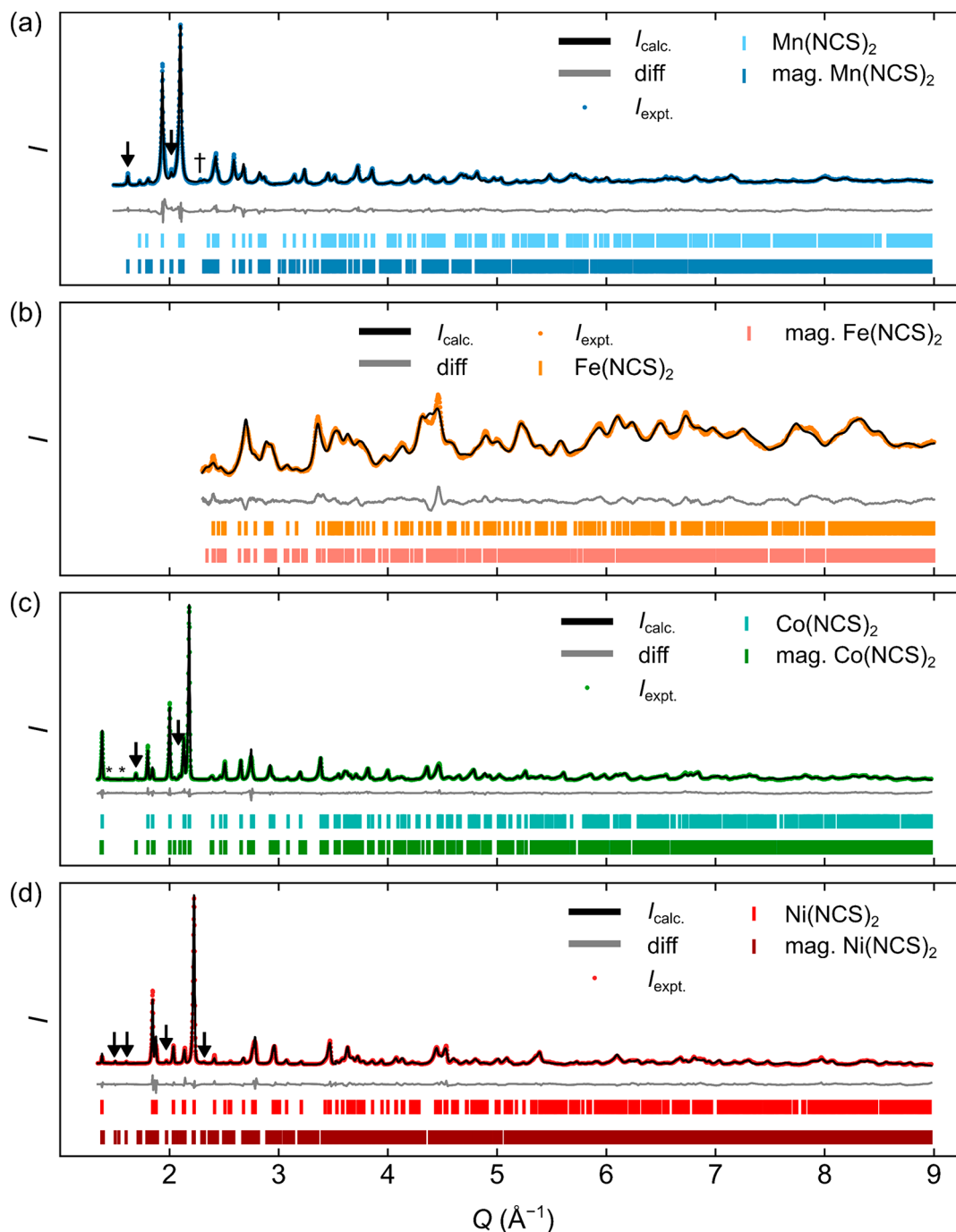


Figure 3. Rietveld refinements of the neutron powder diffraction patterns collected at 1.5 K for $\text{Mn}(\text{NCS})_2$ (a), at 1.5 K for $\text{Co}(\text{NCS})_2$ (c), and 1.5 K for $\text{Ni}(\text{NCS})_2$ (d), all on bank 5 of WISH. (b) Pattern collected at 10 K for $\text{Fe}(\text{NCS})_2$ on bank 5 of GEM. Arrows lie directly above magnetic peaks. Asterisks are directly above magnetic reflections from impurity phases, and daggers are directly above nonmagnetic reflections from impurity phases. $R_{\text{wp}} = 7.54\%$ for $\text{Mn}(\text{NCS})_2$, 2.99% for $\text{Fe}(\text{NCS})_2$, 4.06% for $\text{Co}(\text{NCS})_2$, and 6.25% for $\text{Ni}(\text{NCS})_2$. The low- Q regions of the diffraction patterns are shown in more detail in Figure 8, to emphasize the magnetic Bragg peaks.

hydrates. To confirm whether any solvent remained trapped in the synthesized frameworks, we carried out thermogravimetric analysis (TGA) [Figure S2], which revealed minimal quantities of water lost from each material.

Quantitative Rietveld refinements of the high- Q powder neutron diffraction (PND) data collected confirmed that all four compounds were isostructural [Figure 3], crystallizing in the space group $C2/m$, as anticipated for the similar chemistries and ionic radii of the divalent first row TM cations.⁵⁴

The lattice parameters and atomic coordinates derived from Rietveld refinements are shown in Table 1. The lattice parameters and unit cell volume vary approximately linearly with the cationic radius, r_{ion} [Figure 4]. The b lattice parameter depends only on the M–S bond lengths and M–S–M bond angle and therefore changes proportionately the most as M varies. The observed changes in b are also consistent with the expected differences in M–S bond lengths across the TM series.²¹ The a lattice parameter is dominated by the length of the $(\text{NCS})^-$ anion (which lies along the a axis), rather than the

Table 1. Rietveld-Derived Lattice Parameters and Atomic Coordinates, Based on the Powder Neutron Diffraction Data Collected at 1.5 K for Mn(NCS)₂, Co(NCS)₂, and Ni(NCS)₂ and at 10 K for Fe(NCS)₂^a

Mn(NCS) ₂				
<i>a</i> (Å)	10.8370(17)	α (deg)	90	
<i>b</i> (Å)	3.8824(6)	β (deg)	105.348(2)	
<i>c</i> (Å)	6.2175(9)	γ (deg)	90	
site	<i>x</i>	<i>y</i>	<i>z</i>	
Mn	2 <i>a</i>	0	0	0
N	4 <i>i</i>	−0.1445(2)	0	0.1723(4)
C	4 <i>i</i>	−0.2465(4)	0	0.2278(6)
S	4 <i>i</i>	−0.3743(7)	0	0.2721(11)
Fe(NCS) ₂				
<i>a</i> (Å)	10.630(16)	α (deg)	90	
<i>b</i> (Å)	3.742(6)	β (deg)	105.038(7)	
<i>c</i> (Å)	6.168(10)	γ (deg)	90	
site	<i>x</i>	<i>y</i>	<i>Z</i>	
Fe	2 <i>a</i>	0	0	0
N	4 <i>i</i>	−0.14037(13)	0	0.17658(18)
C	4 <i>i</i>	−0.24139(14)	0	0.2220(2)
S	4 <i>i</i>	−0.3897(3)	0	0.2668(4)
Co(NCS) ₂				
<i>a</i> (Å)	10.6118(4)	α (deg)	90	
<i>b</i> (Å)	3.70869(11)	β (deg)	106.4401(8)	
<i>c</i> (Å)	6.13996(19)	γ (deg)	90	
site	<i>x</i>	<i>y</i>	<i>z</i>	
Co	2 <i>a</i>	0	0	0
N	4 <i>i</i>	−0.13799(7)	0	0.17056(13)
C	4 <i>i</i>	−0.23820(11)	0	0.2171(2)
S	4 <i>i</i>	−0.3782(2)	0	0.2610(4)
Ni(NCS) ₂				
<i>a</i> (Å)	10.5070(5)	α (deg)	90	
<i>b</i> (Å)	3.61889(5)	β (deg)	107.509(3)	
<i>c</i> (Å)	6.16252(16)	γ (deg)	90	
site	<i>x</i>	<i>y</i>	<i>z</i>	
Ni	2 <i>a</i>	0	0	0
N	4 <i>i</i>	−0.1325(2)	0	0.1699(4)
C	4 <i>i</i>	−0.2367(3)	0	0.2086(7)
S	4 <i>i</i>	−0.3778(6)	0	0.2543(9)

^aThe space group for all compounds is C2/m.

M–N and M–S bonds (which are oriented at an angle to the *a* direction) [Figure 1]. Since the length of (NCS)[−] remains approximately constant regardless of the identity of M, changes in M have a small effect on the size of *a*. The *c* lattice parameter remains approximately constant across the series and is determined by the interlayer van der Waals interactions, suggesting these interactions have similar strengths across the first-row TM series.

All compounds except Mn(NCS)₂ were strongly colored microcrystalline powders: Fe(NCS)₂ was orange-brown, Co(NCS)₂ was red-brown,²⁰ Ni(NCS)₂ was green-brown, and Mn(NCS)₂ was pale yellow.²⁷ To quantitatively assess the variation in observed colors across the M(NCS)₂ series, we recorded diffuse reflectance UV–vis spectra [Figure Sa].

The observed intense transitions correspond to ligand-to-metal charge transfer (LMCT) transitions: from states dominated by (NCS)[−]-based orbitals to states dominated by the metal 3d orbitals.^{55–57} The additional weak absorption bands observed for Fe(NCS)₂, Co(NCS)₂, and Ni(NCS)₂

likely correspond to d–d transitions.⁵⁸ The optical (indirect) band gaps were extracted using Tauc fits to the data [Figure Sb],⁵⁹ giving the following values: 4.2(1) eV for Mn(NCS)₂, 3.2(1) eV for Fe(NCS)₂, 3.2(1) eV for Co(NCS)₂, and 2.5(1) eV for Ni(NCS)₂. On moving to later TM ions, the d orbitals decrease in energy and the crystal field splitting increases, resulting in a lower energy (longer wavelength) transition and smaller band gap. This trend is consistent with the small observed band gap for Cu(NCS)₂ (1.3 eV), which is lowered further due to Jahn–Teller distortions of the Cu²⁺ ions.⁹

3.2. Bulk Magnetic Measurements. To assess the change in the magnetic properties as the identity of M in M(NCS)₂ varies, we next went on to measure the bulk magnetic susceptibilities of these compounds at *H* = 0.01 T [Figure 6]. In addition, isothermal magnetization measurements (*M*(*H*) curves) were carried out [Figures S3–S6]; these showed that, in the region −7 to +7 T, saturation is not achieved.

All four compounds showed evidence of three-dimensional antiferromagnetic ordering [Figure 6]: a sharp change in (*dχ*)/(*dT*) at *T*_N and a rapid decrease in χ at low temperatures; in all cases, the ZFC and FC susceptibilities did not diverge [Figure S7]. Each compound also shows a rise in the susceptibility at low temperatures (*T* < 15 K for M = Fe, Co, Ni and *T* < 35 K for M = Mn), due to small amounts (<1 wt %) of paramagnetic impurities and defects, as observed in several other magnetic molecular frameworks.^{9,21,60}

For each compound, the high-temperature magnetic susceptibility (*T* > 150 K) data were fitted to the Curie–Weiss law, yielding values of the Weiss constant, θ , and Curie constant, *C* [Table 2]. The data collected for Ni(NCS)₂ and Co(NCS)₂ are broadly consistent with previously reported measurements.^{20,28} The presence of a significant residual field (<20 Oe) was identified from the isothermal magnetization data [Figures S4–S7]. We have corrected for this field, but it did introduce a significant additional uncertainty. The presence of small quantities of paramagnetic impurities, single-ion anisotropy, and the fact that by necessity we are carrying out a Curie–Weiss fit at *T* < 3| θ | (for Fe(NCS)₂ and Mn(NCS)₂) will also introduce additional small, systematic errors in the fitted parameters.

The large deviations in μ_{eff} from the spin-only values for Fe(NCS)₂ and Co(NCS)₂ likely arise from spin–orbit coupling, due to the residual orbital angular momentum in the ⁵T_{2g} and ⁴T_{1g} terms for high-spin octahedral Fe²⁺ and Co²⁺, respectively.^{61–64} The observed deviations for Mn(NCS)₂ and Ni(NCS)₂ are much smaller, as no first-order orbital contribution is expected.^{65,66}

We note that net magnetic interactions, as measured by θ , become increasingly antiferromagnetic on moving to earlier TM ions [Figure 7], likely due to the more diffuse nature of M²⁺ 3d orbitals earlier in the series, enabling better spatial overlap with the (NCS)[−] σ and π frontier orbitals. The trend in Weiss constants also highlights the considerable increase in the net magnetic interaction strength between spins on moving to earlier TM ions, particularly for Mn(NCS)₂ and Fe(NCS)₂.

As M(NCS)₂ are layered materials with weak van der Waals interactions between the layers, we anticipated these materials would display low-dimensional magnetic behavior. The ratio *f* = | θ |/*T*_N was computed for each compound, as this parameter may be used to assess the extent to which long-range order is suppressed by low-dimensionality or spin frustration.¹⁶ For Mn(NCS)₂, *f* = 4.1(1); for Fe(NCS)₂, *f* = 0.99(4); for

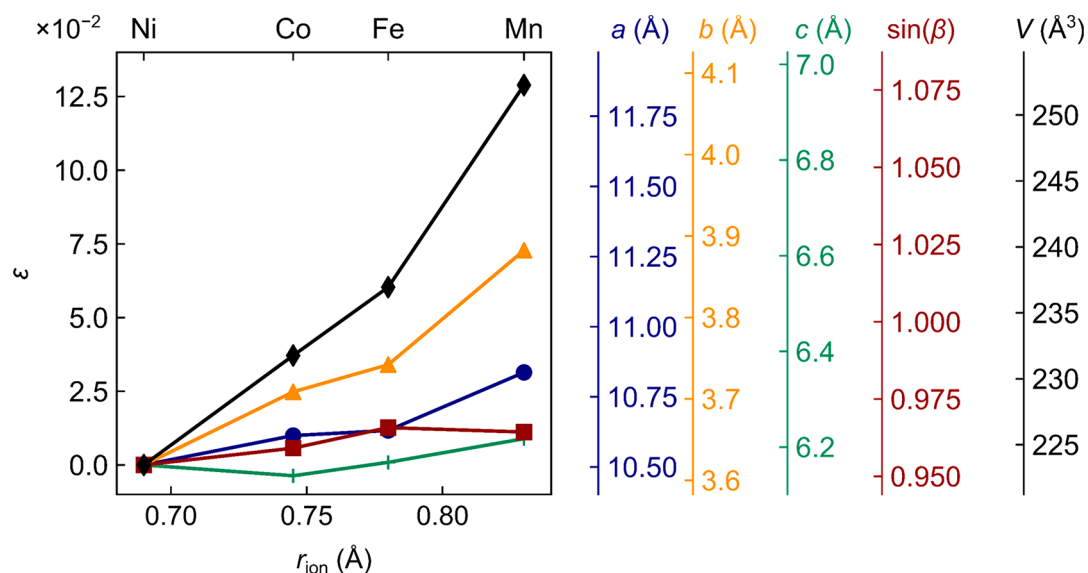


Figure 4. Variation in the strain of Rietveld-derived PND lattice parameters and nuclear unit cell volume (at the base temperature of PND results) with the ionic radius of M^{2+} , r_{ion} . The strain in each parameter, x ($x = a, b, c, \sin(\beta), V$), is calculated via $\epsilon = (x - x_{\text{Ni}})/x_{\text{Ni}}$ —i.e., the strain is calculated relative to the parameters obtained for $\text{Ni}(\text{NCS})_2$. The corresponding values of the lattice parameters are shown on the right-hand axes.

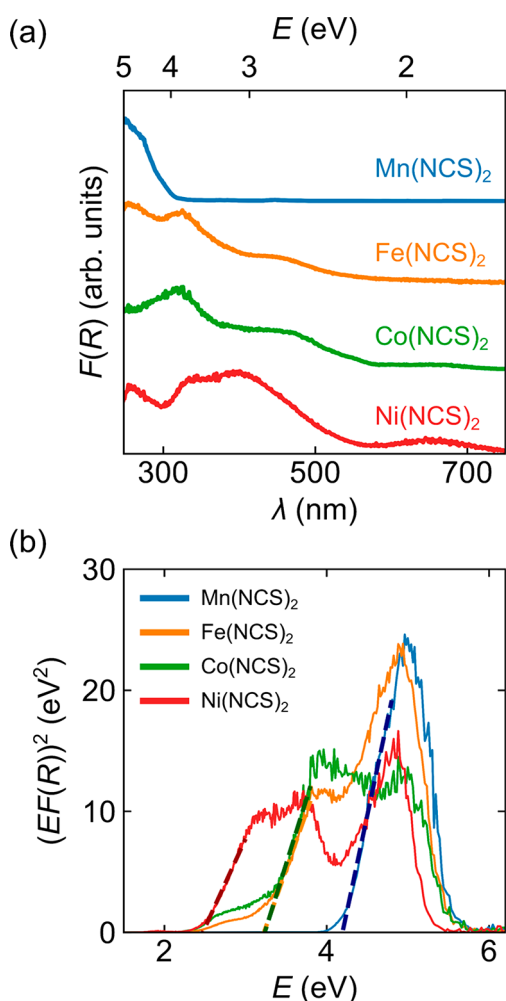


Figure 5. (a) Diffuse reflectance spectra for $M(\text{NCS})_2$ ($M = \text{Mn}, \text{Fe}, \text{Co}, \text{Ni}$). (b) Tauc plots of the diffuse reflectance data: extrapolation of the data to $(F(R)h\nu)^2 = 0$ (indicated by the dashed line) yields the band gap for each material.

$\text{Co}(\text{NCS})_2$, $f = 2.2(1)$; and for $\text{Ni}(\text{NCS})_2$, $f = 0.54(3)$, which do not suggest strong suppression of long-range order.¹⁶

The observed variation in susceptibility below T_N was modeled using a powder-average mean-field theory (MFT) model with Heisenberg exchange [Figure 6].^{67,68} This model qualitatively accounted for the observed magnetic susceptibilities but could not be used to extract the three nearest neighbor exchange interaction strengths, J_1 , J_2 , and J_3 [Figure 2b], as these parameters are correlated. We then attempted to determine the values of J_1 , J_2 , and J_3 using a reaction-field model.⁶⁹ However, this proved unsuccessful, as strong correlations between the parameters again precluded their reliable determination.

3.3. Magnetic Ground State from Neutron Diffraction Experiments. The dominant magnetic interactions in the $M(\text{NCS})_2$ frameworks may be understood by examining their ordered magnetic structures. As such, we carried out low-temperature neutron diffraction experiments to determine the magnetic ground state of these frameworks. All four compounds were observed to adopt ordered commensurate ground states.

On cooling $\text{Mn}(\text{NCS})_2$ below T_N ($= 28$ K), superlattice reflections were observed, corresponding to a propagation vector $\mathbf{k} = [100]^*$. Similarly, for $\text{Fe}(\text{NCS})_2$ and $\text{Co}(\text{NCS})_2$, superlattice reflections corresponding to the $\mathbf{k} = [100]^*$ propagation vector were observed below $T_N = 80$ and 22 K, respectively [Figures 8a,c,e, S8, S9, and S10]; the temperature dependence of these peaks' intensities is shown in Figure 8b, d, and f. This propagation vector corresponds to breaking of the lattice C-centering, leading to a primitive magnetic cell which is twice the size of the primitive nuclear cell.

Symmetry-mode analysis was used to determine the symmetry-allowed magnetic irreducible representations (irreps), yielding mY_1^+ and mY_2^+ irreps, in Miller and Love's notation,⁷⁰ for $\text{Mn}(\text{NCS})_2$, $\text{Fe}(\text{NCS})_2$, and $\text{Co}(\text{NCS})_2$. Rietveld refinement of the data using these irreps revealed that only the mY_2^+ irrep was consistent with the data for $\text{Mn}(\text{NCS})_2$, $\text{Fe}(\text{NCS})_2$, and $\text{Co}(\text{NCS})_2$. The refinements against the mY_2^+ symmetry-adapted mode yielded staggered

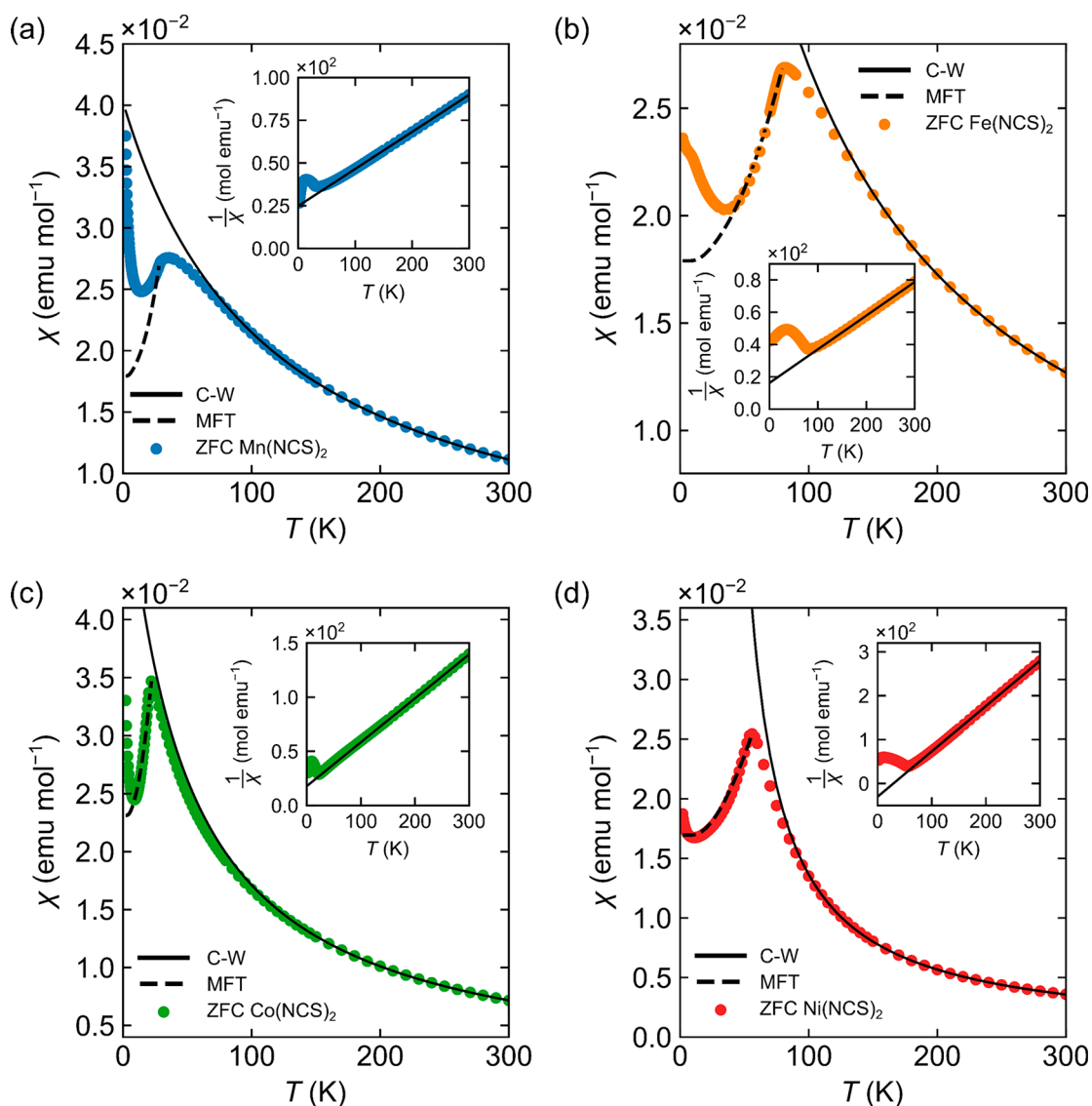


Figure 6. Zero-field cooled (ZFC) magnetic susceptibility data collected for $\text{Mn}(\text{NCS})_2$ (a), $\text{Fe}(\text{NCS})_2$ (b), $\text{Co}(\text{NCS})_2$ (c) and $\text{Ni}(\text{NCS})_2$ (d) in a constant magnetic field strength $H = 0.01$ T. The Curie–Weiss law was used to model the high-temperature ($T > 150$ K) data, while a low-temperature mean-field theory (MFT) model was used for the data $T < T_N$. Insets show the inverse of magnetic susceptibility, used to examine the Curie–Weiss law fit.

Table 2. Bulk Magnetic Susceptibility Parameters, Extracted from the Raw Magnetic Susceptibility Data (T_N), High-Temperature Curie-Weiss Law Fits (θ , μ_{eff} and g), and Rietveld Refinements of the Low-Temperature PND Data (Staggered Moments, m_{sta})^a

	$\text{Mn}(\text{NCS})_2$	$\text{Fe}(\text{NCS})_2$	$\text{Co}(\text{NCS})_2$	$\text{Ni}(\text{NCS})_2$
θ (K)	−115(3)	−78(3)	−44(1)	+29(1)
T_N (K)	28.0(3)	78.4(3)	20.0(5)	54(2)
μ_{eff} (μ_B)	6.4(5)	6.2(5)	4.4(5)	2.8(5)
g	2.2(2)	2.5(2)	2.3(2)	2.0(2)
$m_{\text{sta.}}$ (μ_B)	4.02(4)	4.95(6)	3.02(2)	1.75(5)

^aExperimental standard errors are given in parentheses.

magnetic moments of 4.02(4) μ_B ($\text{Mn}(\text{NCS})_2$), 4.95(6) μ_B ($\text{Fe}(\text{NCS})_2$), and 3.018(16) μ_B ($\text{Co}(\text{NCS})_2$), with magnetic space group P_{A21}/c in the BNS notation.⁷¹

In contrast to the other members of the $\text{M}(\text{NCS})_2$ family, the magnetic Bragg peaks observed below $T_N = 56$ K for

$\text{Ni}(\text{NCS})_2$ were indexed to a propagation vector of $\mathbf{k} = [00\frac{1}{2}]^*$, corresponding to $m_{A_1^+}$ and $m_{A_2^+}$ irreps. The neutron diffraction data were consistent with the $m_{A_2^+}$ -distorted structure and Rietveld refinement against this structure [Figures 8g and S11] yielded a staggered moment of 1.73(5) μ_B and a magnetic space group C_2/c in the BNS notation, with the magnetic unit cell doubled along the c direction, relative to the nuclear cell [Figure 9].

Since $\text{Ni}(\text{NCS})_2$ is ferromagnetic within the layer, we anticipate $J_1/J_2 > -0.5$ and $J_2 < 0$ (i.e., ferromagnetic), so that $\text{Ni}(\text{NCS})_2$ lies in the FM region of the classical phase diagram [Figure 2a]. Likewise, we anticipate $J_1/J_2 < 0.5$ and $J_2 > 0$ for $\text{Mn}(\text{NCS})_2$, $\text{Fe}(\text{NCS})_2$, and $\text{Co}(\text{NCS})_2$, so that these materials occupy the AF region of the classical phase diagram [Figure 2a]. Additional constraints on the relative sizes and signs of J_1 and J_2 are established in the Discussion.

The staggered moments of $\text{Fe}(\text{NCS})_2$, $\text{Co}(\text{NCS})_2$, and $\text{Ni}(\text{NCS})_2$ are broadly consistent with the effective magnetic moments measured via bulk magnetic susceptibility measure-

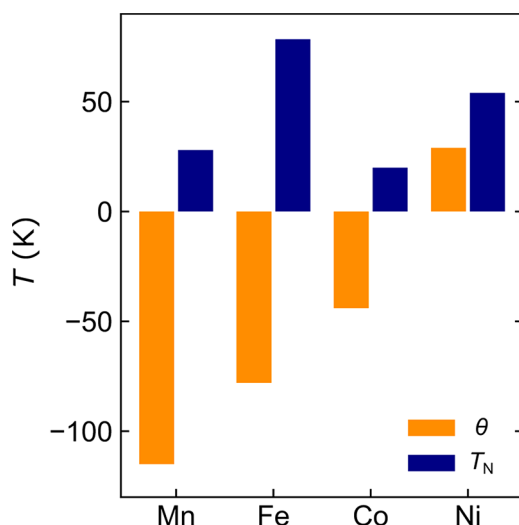


Figure 7. Variation of the Weiss temperature, θ , and Néel temperature, T_N , across the first-row transition metals, M , in the $M(\text{NCS})_2$ family.

ments [Table 2], with deviations from the spin-only values likely arising from delocalization (covalency) effects (see Discussion).

We also established the temperature dependence of the lattice parameters [Figure S12]. For all members of the $M(\text{NCS})_2$ family, the lattice parameters were observed to vary broadly linearly with temperature, with no discontinuities observed. For $\text{Mn}(\text{NCS})_2$, $\text{Co}(\text{NCS})_2$, and $\text{Ni}(\text{NCS})_2$, the c axis expands most as temperature rises [Figure S12], since the interactions along the c axis are primarily weaker van der Waals interactions between the layers. The temperature dependence of lattice parameters for $\text{Fe}(\text{NCS})_2$ could not be accurately determined, due to the breadth of the Bragg peaks (a consequence of the low crystallinity of the sample).

4. DISCUSSION

The divalent first-row TM thiocyanates $M(\text{NCS})_2$ ($M = \text{Mn}$, Fe , Co , and Ni) adopt the same layered crystal structure, with space group $C2/m$. As M changes, we observe broadly linear variations in the lattice parameters with the ionic radius of M^{2+} .

As earlier first-row TM ions occupy the M^{2+} sites in the $M(\text{NCS})_2$ structure, θ becomes increasingly antiferromagnetic [Figure 7], due to (individually) stronger antiferromagnetic interactions and/or weaker ferromagnetic interactions. We expect that the magnetic properties of the $M(\text{NCS})_2$ lattices are dominated by the two nearest neighbor superexchange interactions, J_1 and J_2 . The dipolar interactions between M^{2+} are expected to be small, due to the large distances between M^{2+} centers (at least 3.6 Å, corresponding to a dipolar interaction strength on the order of 0.01 K); likewise, we expect direct exchange to be weak, due to the large M^{2+} – M^{2+} distances. The interlayer interaction, J_3 , will also likely be significantly smaller than the intralayer interactions, due to the large separation and lack of chemical bonds between M^{2+} ions. The observed interlayer S...S contacts are comparable to those of other van der Waals magnetic materials which are well-described by low-dimensional Hamiltonians.^{32–35,43–45}

Therefore, we expect the strengths of the dominant exchange interactions in $M(\text{NCS})_2$ (J_1 and J_2) to depend primarily on the occupation of the magnetic 3d orbitals and their overlap with the frontier orbitals on $(\text{NCS})^-$. In all cases,

we expect the antibonding orbitals generated from this overlap to be the highest occupied orbitals, and therefore these will be the orbitals which dominate the magnetic exchange interactions in $M(\text{NCS})_2$.⁷²

The J_1 interaction will likely contain two contributions: first, antiferromagnetic superexchange involving overlap between t_{2g} and e_g orbitals on adjacent M^{2+} ions (mediated by a S p -like orbital, Figure 10a) and, second, ferromagnetic exchange-correlation-driven superexchange mediated by the two orthogonal sulfur p -like orbitals [Figure 10c].^{73–75} The antiferromagnetic component will weaken from left to right across the TM series, as the number of unpaired electrons in t_{2g} orbitals decreases, until for $M = \text{Ni}$, the t_{2g} orbitals are fully occupied and we anticipate a negligible antiferromagnetic component. Each metal has the same e_g orbital occupation (e_g^2), and so we expect the ferromagnetic contribution [Figure 10c] to be broadly similar in magnitude across the series. Consequently, we expect the J_1 interaction to become increasingly ferromagnetic (more negative J_1) for later TMs.

The J_2 superexchange interaction is principally mediated via the σ - and π -like frontier orbitals on $(\text{NCS})^-$, dominated by lobes on S and N atoms [Figure 10 b and d].⁹ An antiferromagnetic contribution will arise from delocalization superexchange between metal t_{2g} and e_g orbitals via the σ -like frontier orbital on $(\text{NCS})^-$ [Figure 10b]. A countervailing ferromagnetic interaction will be produced by exchange correlation between the metal e_g orbitals on M^{2+} , mediated by the orthogonal σ - and π -like frontier orbitals on $(\text{NCS})^-$ [Figure 10d]. Again, as electrons are added to the t_{2g} orbitals (from Mn^{2+} to Ni^{2+}), the antiferromagnetic component of the J_2 interaction will weaken and become negligible for $M = \text{Ni}$, resulting in a more ferromagnetic J_2 . Indeed, for many $M(\text{NCS})_2$ solvate frameworks (those of the form $M(\text{NCS})_2L_x$, where $L = \text{ligand}$), the Ni member of the family orders ferromagnetically along the Ni–NCS–Ni chains, while the Mn and Co members order antiferromagnetically,^{23,25,60,76,77} consistent with our experimental results and proposed magnetochemical mechanisms.

This rationalization can only provide a general understanding of the magnetic behavior of these materials. Deviations from the “ideal” 90° M–S–M and 180° M–(NCS)–M bond angles, will likely mix the ferromagnetic and antiferromagnetic components of each interaction, giving deviations from the trends we explain above. In addition, changes in the size and energy match of the metal 3d and $(\text{NCS})^-$ orbitals, along with spin–orbit effects, will play a key role in determining the strength of the interactions in these materials.

Furthermore, we expect that single-ion properties will play a significant role in the behavior of $\text{Co}(\text{NCS})_2$, $\text{Ni}(\text{NCS})_2$, and $\text{Fe}(\text{NCS})_2$, producing deviations both from classical two-dimensional Heisenberg behavior and in the measured value of θ . Nevertheless, our qualitative predictions of the signs and strengths of the J_1 and J_2 interactions are borne out by the observed magnetic ground states and trends in the bulk magnetic properties.

We anticipate that these materials will show similar magnetic behavior to two-dimensional systems, despite ordering as bulk antiferromagnets, as we expect the interlayer interactions (J_3) to be weak. Therefore, our magnetochemical model allows us to rationalize the location of each compound in the classical two-dimensional magnetic phase diagram [Figure 2a]. For $M = \text{Mn}$, Fe , and Co , we expect $J_2 > 0$ (i.e., antiferromagnetic),

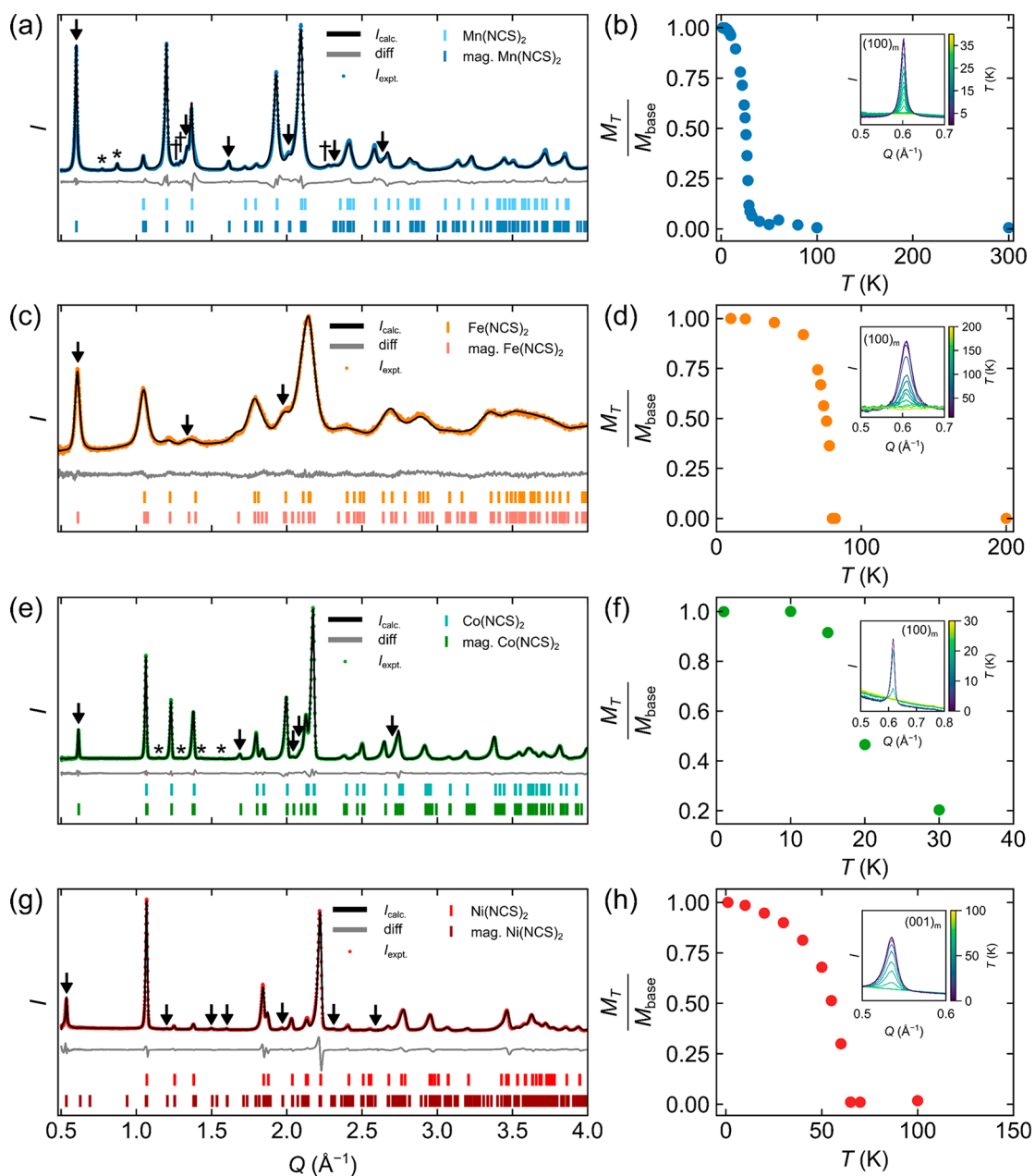


Figure 8. Rietveld fits to the PND patterns between $Q = 0.48 \text{ \AA}^{-1}$ and $Q = 4.00 \text{ \AA}^{-1}$ collected at 1.5 K for $\text{Mn}(\text{NCS})_2$ (a), at 1.5 K for $\text{Co}(\text{NCS})_2$ (e), and at 1.5 K for $\text{Ni}(\text{NCS})_2$ (g), all on bank 2 of WISH. (c) PND pattern for $\text{Fe}(\text{NCS})_2$ collected at 10 K on bank 2 of GEM. Arrows lie directly above magnetic reflections from magnetically ordered $\text{M}(\text{NCS})_2$; asterisks are directly above reflections from magnetic impurities, while daggers are directly above reflections from nonmagnetic impurities. $R_{\text{wp}} = 7.54\%$ for $\text{Mn}(\text{NCS})_2$, 2.99% for $\text{Fe}(\text{NCS})_2$, 4.06% for $\text{Co}(\text{NCS})_2$, and 6.25% for $\text{Ni}(\text{NCS})_2$. b, d, f, and h show how the reduced staggered moment (M_T/M_{base} , where M_T is the moment at temperature T and M_{base} the base temperature moment; all moments were obtained from the Rietveld fits) varies as a function of temperature for $\text{Mn}(\text{NCS})_2$, $\text{Fe}(\text{NCS})_2$, $\text{Co}(\text{NCS})_2$, and $\text{Ni}(\text{NCS})_2$, respectively. Insets show how the intensities of the magnetic (100) peaks for $\text{Mn}(\text{NCS})_2$, $\text{Fe}(\text{NCS})_2$, and $\text{Co}(\text{NCS})_2$ and the magnetic (001) peak for $\text{Ni}(\text{NCS})_2$ vary as a function of temperature.

while we expect J_1 to be small and either ferromagnetic or antiferromagnetic, due to cancellation of the superexchange contributions. This predicts that these materials all lie in the AF region of the phase diagram, as observed from their ground state magnetic structures. As J_1 becomes more antiferromagnetic, we anticipate moderate geometric frustration with the antiferromagnetic J_2 , and indeed f is largest for $\text{Mn}(\text{NCS})_2$. For $M = \text{Ni}$, we anticipate J_1 and J_2 to be ferromagnetic (i.e., $J_1, J_2 < 0$), placing it in the FM region of the phase diagram, as observed.

For all members of the $\text{M}(\text{NCS})_2$ family, the size of the staggered moments obtained from PND are all lower than the size of the expected maximum ordered moment (i.e., gS). This likely arises from the effects of covalency, where spin density is transferred from M^{2+} to the $(\text{NCS})^-$ ligand,⁷⁸ and from contributions from the orbital moment.

Finally, we find that the ordered moment lies broadly along the N–M–N axis for $\text{Mn}(\text{NCS})_2$ and $\text{Ni}(\text{NCS})_2$, suggesting significant spin density in the d orbital pointing along that axis. For $\text{Fe}(\text{NCS})_2$ and $\text{Co}(\text{NCS})_2$, the moment has a significant tilt away from the N–M–N axis, toward the meridional plane

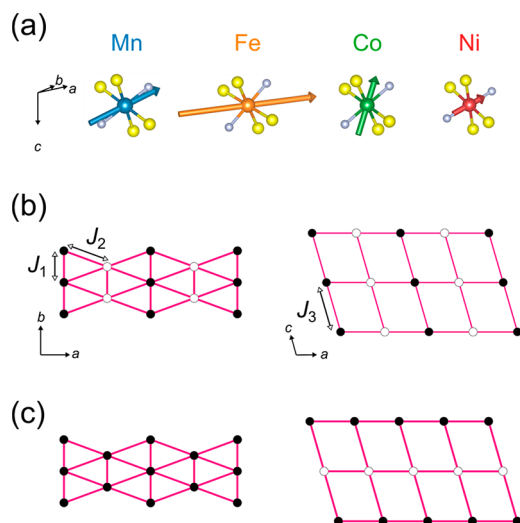


Figure 9. (a) Schematic of the ordered magnetic moments of Mn^{2+} , Fe^{2+} , Co^{2+} , and Ni^{2+} in $\text{M}(\text{NCS})_2$ (N atoms in gray-blue, S in yellow). The magnetic lattice adopted by $\text{Mn}(\text{NCS})_2$, $\text{Fe}(\text{NCS})_2$, and $\text{Co}(\text{NCS})_2$ is shown in b, while c shows the magnetic lattice of $\text{Ni}(\text{NCS})_2$. Filled and empty circles denote collinear moments with opposite spatial orientations.

containing S-bound $(\text{NCS})^-$ ligands, suggesting the important role of spin–orbit effects. Future electron spin resonance

spectroscopy will shed further light on the origin of these differences by providing more precise estimates of g and the superexchange interactions, respectively.

Recent work on CrI_3 and $\text{Cr}_2\text{Ge}_2\text{Te}_6$ has shown that mechanical exfoliation of layered ferromagnets can generate single-layer magnets.^{79–81} While bulk $\text{Ni}(\text{NCS})_2$ orders as a three-dimensional antiferromagnet, the combination of ferromagnetic intralayer order with weak interlayer interactions suggests that monolayers of this may host single-layer ferromagnetism, provided there is sufficient anisotropy. These single-layer ferromagnets may have applications as magnetoelectronic devices, ferromagnetic light emitters,^{79,80} and hybrid multilayer materials,^{82,83} motivating future synthetic studies.

5. CONCLUSION

In this work, we have determined how the strengths of magnetic interactions vary across the first-row TM pseudobinary thiocyanates, $\text{M}(\text{NCS})_2$. Two new materials— $\text{Mn}(\text{NCS})_2$ and $\text{Fe}(\text{NCS})_2$ —are reported, alongside the magnetic structures of these materials and of $\text{Co}(\text{NCS})_2$ and $\text{Ni}(\text{NCS})_2$. On the basis of the observed magnetic structures, we have qualitatively rationalized the relative strengths and signs of the nearest-neighbor in-plane exchange interactions, J_1 and J_2 , and have located each material on the magnetic phase diagram of the spatially anisotropic triangular lattice.

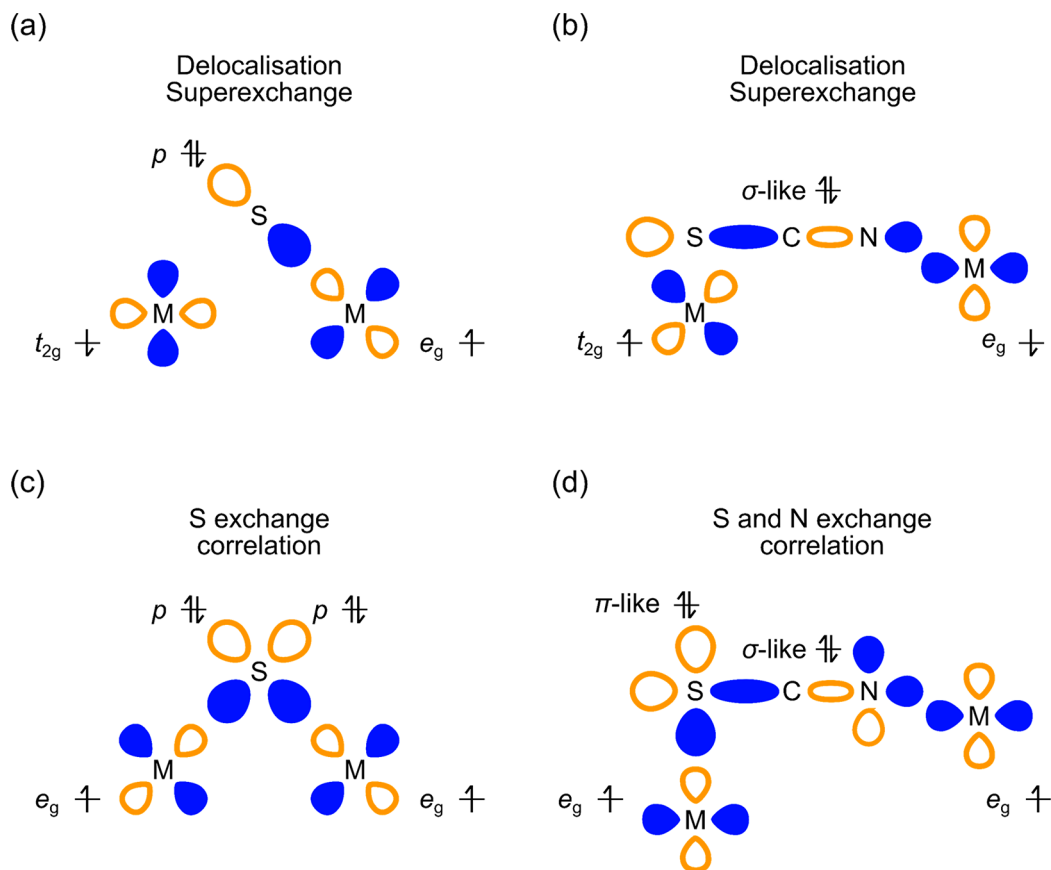


Figure 10. Schematic figures illustrating simplified superexchange mechanisms for the J_1 (a and c) and J_2 (b and d) interactions in terms of the magnetic M^{2+} 3d orbitals and frontier σ -like and π -like orbitals on $(\text{NCS})^-$. Orange and blue lobes indicate opposite phases of orbital wave functions. The antiferromagnetic components of the J_1 (a) and J_2 (b) interactions proceed via delocalization superexchange, while the ferromagnetic components proceed via exchange correlation—either via S only for J_1 (c) or via S and N for J_2 (d).

On moving to TM ions earlier in the row, the net magnetic interactions become stronger and increasingly antiferromagnetic, with the Weiss constant reaching $-115(3)$ K for $\text{Mn}(\text{NCS})_2$ and the Néel temperature of $\text{Fe}(\text{NCS})_2$ reaching above 78 K.

PND revealed that $\text{Mn}(\text{NCS})_2$, $\text{Fe}(\text{NCS})_2$, and $\text{Co}(\text{NCS})_2$ adopt the same commensurate antiferromagnetic structure, in which parallel spins along the crystallographic b axis order antiferromagnetically along the a axis; these layers of spins are then stacked antiferromagnetically along the c direction. In contrast, the magnetic structure of $\text{Ni}(\text{NCS})_2$ comprises ferromagnetically ordered ab layers ordered antiferromagnetically along the c axis. This suggests that single-layer $\text{Ni}(\text{NCS})_2$ may be a candidate monolayer ferromagnet belonging to a new family of magnetic frameworks. The results collected from this study open up new avenues for the rational design of magnetic molecular framework materials.

■ ASSOCIATED CONTENT

SI Supporting Information

The Supporting Information is available free of charge at <https://pubs.acs.org/doi/10.1021/acs.inorgchem.0c01478>.

Additional experimental details, including powder X-ray diffraction, TGA, isothermal magnetization, powder neutron diffraction, and variable temperature powder neutron diffraction data (PDF)

Accession Codes

CCDC 2006184–2006187 contain the supplementary crystallographic data for this paper. These data can be obtained free of charge via www.ccdc.cam.ac.uk/data_request/cif, or by emailing data_request@ccdc.cam.ac.uk, or by contacting The Cambridge Crystallographic Data Centre, 12 Union Road, Cambridge CB2 1EZ, UK; fax: +44 1223 336033.

■ AUTHOR INFORMATION

Corresponding Authors

Clare P. Grey – Department of Chemistry, University of Cambridge, Cambridge CB2 1EW, United Kingdom; orcid.org/0000-0001-5572-192X; Email: cpg27@cam.ac.uk

Matthew J. Cliffe – Department of Chemistry, University of Cambridge, Cambridge CB2 1EW, United Kingdom; School of Chemistry, Nottingham NG7 2RD, United Kingdom; orcid.org/0000-0002-0408-7647; Email: matthew.cliffe@nottingham.ac.uk

Authors

Euan N. Bassey – Department of Chemistry, University of Cambridge, Cambridge CB2 1EW, United Kingdom; orcid.org/0000-0001-8827-7175

Joseph A. M. Paddison – Churchill College and Cavendish Laboratory, Department of Physics, University of Cambridge, Cambridge CB3 0DS, United Kingdom; Materials Science & Technology Division, Oak Ridge National Laboratory, Oak Ridge, Tennessee 37831, United States of America

Evan N. Keyzer – Department of Chemistry, University of Cambridge, Cambridge CB2 1EW, United Kingdom

Jeongjae Lee – Department of Chemistry, University of Cambridge, Cambridge CB2 1EW, United Kingdom; School of Earth and Environmental Sciences, Seoul National University, Seoul 08826, Korea

Pascal Manuel – ISIS Facility, STFC Rutherford Appleton Laboratory, Didcot OX11 0QX, United Kingdom

Ivan da Silva – ISIS Facility, STFC Rutherford Appleton Laboratory, Didcot OX11 0QX, United Kingdom

Siân E. Dutton – Cavendish Laboratory, Department of Physics, University of Cambridge, Cambridge CB3 0HE, United Kingdom; orcid.org/0000-0003-0984-5504

Complete contact information is available at: <https://pubs.acs.org/doi/10.1021/acs.inorgchem.0c01478>

Notes

The authors declare no competing financial interest.

■ ACKNOWLEDGMENTS

E.N.B. thanks the EPSRC for financial support. J.A.M.P.'s work at Cambridge was supported by Churchill College, University of Cambridge. J.A.M.P.'s work at Oak Ridge National Laboratory (ORNL) was supported by the Laboratory Directed Research and Development Program of ORNL, managed by UT-Battelle, LLC for the US Department of Energy (discussion of magnetic modelling) and the U.S. Department of Energy, Office of Science, Basic Energy Sciences, Materials Sciences and Engineering Division (computational resources). E.N.K. thanks NSERC of Canada for a PGSD. J.L. thanks Trinity College, University of Cambridge for financial support. M.J.C. acknowledges the School of Chemistry, University of Nottingham for a Hobday Fellowship. Magnetic measurements were carried out using the Advanced Materials Characterisation Suite, funded by EPSRC Strategic Equipment Grant EP/M000524/1. We also acknowledge the Rutherford Appleton Laboratory for access to the ISIS Neutron Source.

■ REFERENCES

- (1) Ramesh, R. Emerging Routes to Multiferroics. *Nature* **2009**, *461* (7268), 1218–1219.
- (2) Stroppa, A.; Barone, P.; Jain, P.; Perez-Mato, J. M.; Picozzi, S. Hybrid Improper Ferroelectricity in a Multiferroic and Magneto-electric Metal-Organic Framework. *Adv. Mater.* **2013**, *25* (16), 2284–2290.
- (3) Boström, H. L. B.; Senn, M. S.; Goodwin, A. L. Recipes for Improper Ferroelectricity in Molecular Perovskites. *Nat. Commun.* **2018**, *9* (1), 2380.
- (4) Wang, Z.; Jain, P.; Choi, K.-Y.; Van Tol, J.; Cheetham, A. K.; Kroto, H. W.; Koo, H.-J.; Zhou, H.; Hwang, J.; Choi, E. S.; Whangbo, M.-H.; Dalal, N. S. Dimethylammonium Copper Formate $[(\text{CH}_3)_2\text{NH}_2]\text{Cu}(\text{HCOO})_3$: A Metal-Organic Framework with Quasi-One-Dimensional Antiferromagnetism and Magnetostriction. *Phys. Rev. B: Condens. Matter Mater. Phys.* **2013**, *87* (22), 224406.
- (5) Maspoch, D.; Ruiz-Molina, D.; Veciana, J. Magnetic Nanoporous Coordination Polymers. *J. Mater. Chem.* **2004**, *14* (18), 2713–2723.
- (6) Motokawa, N.; Matsunaga, S.; Takaishi, S.; Miyasaka, H.; Yamashita, M.; Dunbar, K. R. Reversible Magnetism between an Antiferromagnet and a Ferromagnet Related to Solvation/Desolvation in a Robust Layered $[\text{Ru}_2]_2\text{TCNQ}$ Charge-Transfer System. *J. Am. Chem. Soc.* **2010**, *132*, 11943–11951.
- (7) Maspoch, D.; Ruiz-Molina, D.; Wurst, K.; Domingo, N.; Cavallini, M.; Biscarini, F.; Tejada, J.; Rovira, C.; Veciana, J. A Nanoporous Molecular Magnet with Reversible Solvent-Induced Mechanical and Magnetic Properties. *Nat. Mater.* **2003**, *2* (3), 190–195.
- (8) Cairns, A. B.; Goodwin, A. L. Structural Disorder in Molecular Framework Materials. *Chem. Soc. Rev.* **2013**, *42* (12), 4881.
- (9) Cliffe, M. J.; Lee, J.; Paddison, J. A. M.; Schott, S.; Mukherjee, P.; Gaultois, M. W.; Manuel, P.; Siringhaus, H.; Dutton, S. E.; Grey, C.

- P. Low-Dimensional Quantum Magnetism in $\text{Cu}(\text{NCS})_2$, a Molecular Framework Material. *Phys. Rev. B: Condens. Matter Mater. Phys.* **2018**, *97* (14), 144421.
- (10) Greenfield, J. T.; Kamali, S.; Izquierdo, N.; Chen, M.; Kovnir, K. $\text{NH}_4\text{FeCl}_2(\text{HCOO})$: Synthesis, Structure, and Magnetism of a Novel Low-Dimensional Magnetic Material. *Inorg. Chem.* **2014**, *53* (6), 3162–3169.
- (11) Saines, P. J.; Paddison, J. A. M.; Thygesen, P. M. M.; Tucker, M. G. Searching beyond Gd for Magnetocaloric Frameworks: Magnetic Properties and Interactions of the $\text{Ln}(\text{HCOO})_3$ Series. *Mater. Horiz.* **2015**, *2* (5), 528–535.
- (12) Kurmoo, M.; Kepert, C. J. Hard Magnets Based on Transition Metal Complexes with the Dicyanamide Anion, $\{\text{N}(\text{CN})_2\}^-$. *New J. Chem.* **1998**, *22*, 1515–1524.
- (13) Saines, P. J.; Bristowe, N. C. Probing Magnetic Interactions in Metal-Organic Frameworks and Coordination Polymers Microscopically. *Dalton Transactions*; Royal Society of Chemistry, 2018; Vol 47, pp 13257–13280;
- (14) Böhme, M.; Jochim, A.; Rams, M.; Lohmiller, T.; Suckert, S.; Schnegg, A.; Plass, W.; Näther, C. Variation of the Chain Geometry in Isomeric 1D $\text{Co}(\text{NCS})_2$ Coordination Polymers and Their Influence on the Magnetic Properties. *Inorg. Chem.* **2020**, *59* (8), 5325–5338.
- (15) Dixey, R. J. C.; Saines, P. J. Optimization of the Magnetocaloric Effect in Low Applied Magnetic Fields in LnOHCO_3 Frameworks. *Inorg. Chem.* **2018**, *57* (20), 12543–12551.
- (16) Landee, C. P.; Turnbull, M. M. Review: A Gentle Introduction to Magnetism: Units, Fields, Theory, and Experiment. *J. Coord. Chem.* **2014**, *67* (3), 375–439.
- (17) Balents, L. Spin Liquids in Frustrated Magnets. *Nature* **2010**, *464* (7286), 199–208.
- (18) Wen, J.; Yu, S.-L.; Li, S.; Yu, W.; Li, J.-X. Experimental Identification of Quantum Spin Liquids. *npj Quantum Mater.* **2019**, *4* (1), 12.
- (19) Lee, P. A.; Nagaosa, N.; Wen, X.-G. Doping a Mott Insulator: Physics of High-Temperature Superconductivity. *Rev. Mod. Phys.* **2006**, *78* (1), 17–85.
- (20) Shurdha, E.; Lapidus, S. H.; Stephens, P. W.; Moore, C. E.; Rheingold, A. L.; Miller, J. S. Extended Network Thiocyanate- and Tetracyanoethanide-Based First-Row Transition Metal Complexes. *Inorg. Chem.* **2012**, *51* (18), 9655–9665.
- (21) Shurdha, E.; Moore, C. E.; Rheingold, A. L.; Lapidus, S. H.; Stephens, P. W.; Arif, A. M.; Miller, J. S. First Row Transition Metal(II) Thiocyanate Complexes, and Formation of 1-, 2-, and 3-Dimensional Extended Network Structures of $\text{M}(\text{NCS})_2(\text{Solvent})_2$ ($\text{M} = \text{Cr, Mn, Co}$) Composition. *Inorg. Chem.* **2013**, *52* (18), 10583–10594.
- (22) Reller, A.; Oswald, H. R. Mechanism and Kinetics of Thermal Decompositions of Solids Governed by Phase-Boundary Processes. *J. Solid State Chem.* **1986**, *62* (3), 306–316.
- (23) Boeckmann, J.; Näther, C. Metamagnetism and Long Range Ordering in μ -1,3 Bridging Transition Metal Thiocyanato Coordination Polymers. *Polyhedron* **2012**, *31* (1), 587–595.
- (24) Julve, M.; Verdager, M.; De Munno, G.; Real, J. A.; Bruno, G. Synthesis, Crystal Structure, and Magnetic Properties of (μ -Bipyrimidine)(Cyanato)Copper(II) and-(Thiocyanato)Copper(II) Complexes. *Inorg. Chem.* **1993**, *32* (6), 795–802.
- (25) DeFotis, G. C.; Harlan, E. W.; Remy, E. D.; Dell, K. D. Ferromagnetism of $\text{Ni}(\text{SCN})_2(\text{C}_2\text{H}_5\text{OH})_2$. *J. Appl. Phys.* **1991**, *69*, 6004–6006.
- (26) Dhers, S.; Feltham, H. L. C.; Brooker, S. A Toolbox of Building Blocks, Linkers and Crystallisation Methods Used to Generate Single-Chain Magnets. *Coord. Chem. Rev.* **2015**, *296*, 24–44.
- (27) Dubler, E.; Reller, A.; Oswald, H. R. Intermediates in Thermal Decomposition of Nickel(II) Complexes: The Crystal Structures of $\text{Ni}(\text{SCN})_2(\text{NH}_3)_2$ and $\text{Ni}(\text{SCN})_2$. *Zeitschrift für Krist. – Cryst. Mater.* **1982**, *161* (3–4), 265–278.
- (28) DeFotis, G. C.; Dell, K. D.; Krovich, D. J.; Brubaker, W. W. Antiferromagnetism of $\text{Ni}(\text{SCN})_2$. *J. Appl. Phys.* **1993**, *73* (10), 5386–5388.
- (29) Ramirez, A. P. Strongly Geometrically Frustrated Magnets. *Annu. Rev. Mater. Sci.* **1994**, *24* (1), 453–480.
- (30) Jiang, N.; La Pierre, H. S. Frustrated Magnetism in a 2-D Ytterbium Fluoride. *Inorg. Chem.* **2019**, *58* (18), 12152–12156.
- (31) Tustain, K.; Farrar, L.; Yao, W.; Lightfoot, P.; Da Silva, I.; Telling, M. T. F.; Clark, L. Materialization of a Geometrically Frustrated Magnet in a Hybrid Coordination Framework: A Study of the Iron(II) Oxalate Fluoride Framework, $\text{KFe}(\text{C}_2\text{O}_4)\text{F}$. *Inorg. Chem.* **2019**, *58* (18), 11971–11977.
- (32) Tokunaga, Y.; Okuyama, D.; Kurumaji, T.; Arima, T.; Nakao, H.; Murakami, Y.; Taguchi, Y.; Tokura, Y. Multiferroicity in NiBr_2 with Long-Wavelength Cycloidal Spin Structure on a Triangular Lattice. *Phys. Rev. B: Condens. Matter Mater. Phys.* **2011**, *84* (6), No. 060406.
- (33) Kurumaji, T.; Seki, S.; Ishiwata, S.; Murakawa, H.; Kaneko, Y.; Tokura, Y. Magnetolectric Responses Induced by Domain Rearrangement and Spin Structural Change in Triangular-Lattice Helimagnets NiI_2 and CoI_2 . *Phys. Rev. B: Condens. Matter Mater. Phys.* **2013**, *87* (1), No. 014429.
- (34) Kurumaji, T.; Seki, S.; Ishiwata, S.; Murakawa, H.; Tokunaga, Y.; Kaneko, Y.; Tokura, Y. Magnetic-Field Induced Competition of Two Multiferroic Orders in a Triangular-Lattice Helimagnet MnI_2 . *Phys. Rev. Lett.* **2011**, *106* (16), 167206.
- (35) Kuindersma, S. R.; Sanchez, J. P.; Haas, C. Magnetic and Structural Investigations on NiI_2 and CoI_2 . *Physica B+C* **1981**, *111* (2–3), 231–248.
- (36) Bai, X.; Zhang, S.-S.; Dun, Z.; Zhang, H.; Huang, Q.; Zhou, H.; Stone, M. B.; Kolesnikov, A. I.; Ye, F.; Batista, C. D.; Mourigal, M. Hybridized Quadrupolar Excitations in the Spin-Anisotropic Frustrated Magnet FeI_2 . *arXiv:2004.05623*, **2020**.
- (37) Moore, M. W.; Day, P. Magnetic Phase Diagrams and Helical Magnetic Phases in $\text{M}_x\text{Ni}_{(1-x)}\text{Br}_2$ ($\text{M} = \text{Fe, Mn}$): A Neutron Diffraction and Magneto-Optical Study. *J. Solid State Chem.* **1985**, *59* (1), 23–41.
- (38) Lee, C.; Liu, J.; Whangbo, M. H.; Koo, H. J.; Kremer, R. K.; Simon, A. Investigation of the Spin Exchange Interactions and the Magnetic Structure of the High-Temperature Multiferroic CuBr_2 . *Phys. Rev. B: Condens. Matter Mater. Phys.* **2012**, *86* (6), No. 060407.
- (39) Seki, S.; Kurumaji, T.; Ishiwata, S.; Matsui, H.; Murakawa, H.; Tokunaga, Y.; Kaneko, Y.; Hasegawa, T.; Tokura, Y. Cupric Chloride CuCl_2 as an $S = 1/2$ Chain Multiferroic. *Phys. Rev. B: Condens. Matter Mater. Phys.* **2010**, *82* (6), No. 064424.
- (40) Schmidt, B.; Thalmeier, P. Neel Temperature and Reentrant H - T Phase Diagram of Quasi-2D Frustrated Magnets. *Phys. Rev. B: Condens. Matter Mater. Phys.* **2017**, *96*, 214443.
- (41) Schmidt, B.; Thalmeier, P. Quantum Fluctuations in Anisotropic Triangular Lattices with Ferromagnetic and Antiferromagnetic Exchange. *Phys. Rev. B: Condens. Matter Mater. Phys.* **2014**, *89* (18), 184402.
- (42) Gholivand, K.; Farshadfar, K.; Roe, S. M.; Hosseini, M.; Gholami, A. Investigation of Structure-Directing Interactions within Copper(I) Thiocyanate Complexes through X-Ray Analyses and Non-Covalent Interaction (NCI) Theoretical Approach. *CrystEngComm* **2016**, *18* (37), 7104–7115.
- (43) Nakayama, G.; Hara, S.; Sato, H.; Narumi, Y.; Nojiri, H. Synthesis and Magnetic Properties of a New Series of Triangular-Lattice Magnets, $\text{Na}_2\text{BaMV}_2\text{O}_8$ ($\text{M} = \text{Ni, Co, and Mn}$). *J. Phys.: Condens. Matter* **2013**, *25* (11), 116003.
- (44) Susner, M. A.; Chyasnavichyus, M.; McGuire, M. A.; Ganesh, P.; Maksymovych, P. Metal Thio- and Selenophosphates as Multifunctional van Der Waals Layered Materials. *Adv. Mater.* **2017**, *29* (38), 1602852.
- (45) Wang, F.; Shifa, T. A.; Yu, P.; He, P.; Liu, Y.; Wang, F.; Wang, Z.; Zhan, X.; Lou, X.; Xia, F.; He, J. New Frontiers on van Der Waals Layered Metal Phosphorous Trichalcogenides. *Adv. Funct. Mater.* **2018**, *28* (37), 1802151.
- (46) Pawley, G. S. Unit-Cell Refinement from Powder Diffraction Scans. *J. Appl. Crystallogr.* **1981**, *14* (6), 357–361.

- (47) Rietveld, H. M. Line Profiles of Neutron Powder-Diffraction Peaks for Structure Refinement. *Acta Crystallogr.* **1967**, *22* (1), 151–152.
- (48) Rietveld, H. M. A Profile Refinement Method for Nuclear and Magnetic Structures. *J. Appl. Crystallogr.* **1969**, *2* (2), 65–71.
- (49) Coelho, A. A. TOPAS and TOPAS-Academic: An Optimization Program Integrating Computer Algebra and Crystallographic Objects Written in C++. *J. Appl. Crystallogr.* **2018**, *51* (1), 210–218.
- (50) Coelho, A. TOPAS-Academic: General Profile and Structure Analysis Software for Powder Diffraction Data; Brisbane, Australia, 2007.
- (51) Bain, G. A.; Berry, J. F. Diamagnetic Corrections and Pascal's Constants. *J. Chem. Educ.* **2008**, *85* (4), 532–536.
- (52) Chapon, L. C.; Manuel, P.; Radaelli, P. G.; Benson, C.; Perrott, L.; Ansell, S.; Rhodes, N. J.; Raspino, D.; Duxbury, D.; Spill, E.; Norris, J. Wish: The New Powder and Single Crystal Magnetic Diffractometer on the Second Target Station. *Neutron News* **2011**, *22* (2), 22–25.
- (53) Arnold, O.; Bilheux, J. C.; Borreguero, J. M.; Buts, A.; Campbell, S. I.; Chapon, L.; Doucet, M.; Draper, N.; Ferraz Leal, R.; Gigg, M. A.; Lynch, V. E.; Markvardsen, A.; Mikkelsen, D. J.; Mikkelsen, R. L.; Miller, R.; Palmen, K.; Parker, P.; Passos, G.; Perring, T. G.; Peterson, P. F.; Ren, S.; Reuter, M. A.; Savici, A. T.; Taylor, J. W.; Taylor, R. J.; Tolchenov, R.; Zhou, W.; Zikovsky, J. Mantid—Data Analysis and Visualization Package for Neutron Scattering and μ SR Experiments. *Nucl. Instrum. Methods Phys. Res., Sect. A* **2014**, *764*, 156–166.
- (54) Shannon, R. D. Revised Effective Ionic Radii and Systematic Studies of Interatomic Distances in Halides and Chalcogenides. *Acta Crystallogr., Sect. A: Cryst. Phys., Diffraction, Theor. Gen. Crystallogr.* **1976**, *32* (5), 751–767.
- (55) Cliffe, M. J.; Keyzer, E. N.; Dunstan, M. T.; Ahmad, S.; De Volder, M. F. L.; Deschler, F.; Morris, A. J.; Grey, C. P. Strongly Coloured Thiocyanate Frameworks with Perovskite-Analogue Structures. *Chem. Sci.* **2019**, *10* (3), 793–801.
- (56) Addison, A. W.; Butcher, R. J.; Homonnay, Z.; Pavlishchuk, V. V.; Prushan, M. J.; Thompson, L. K. The Hexakis(Thiocyanato)-Ferrate(III) Ion: A Coordination Chemistry Classic Reveals an Interesting Geometry Pattern for the Thiocyanate Ligands. *Eur. J. Inorg. Chem.* **2005**, *2005* (12), 2404–2408.
- (57) Dinsdale, D. R.; Lough, A. J.; Lemaire, M. T. Structure and Magnetic Properties of an Unusual Homoleptic Iron(III) Thiocyanate Dimer. *Dalt. Trans.* **2015**, *44* (24), 11077–11082.
- (58) Rosseinsky, D. R.; Dorrity, I. A. Ligand Field Parameters and Spectra of First-Row Transition Metal Dihalides in the Solid State. *Coord. Chem. Rev.* **1978**, *25* (1), 31–67.
- (59) Tauc, J. Optical Properties and Electronic Structure of Amorphous Ge and Si. *Mater. Res. Bull.* **1968**, *3* (1), 37–46.
- (60) Wöhlert, S.; Fink, L.; Schmidt, M. U.; Näther, C. Synthesis and Characterization of New 2D Coordination Polymers Based on $\text{Mn}(\text{NCS})_2$ and $\text{Ni}(\text{NCS})_2$ with 1, 2-Bis(4-Pyridyl)-Ethane as Co-Ligand. *Z. Anorg. Allg. Chem.* **2013**, *639* (12–13), 2186–2194.
- (61) Tanabe, Y.; Sugano, S. On the Absorption Spectra of Complex Ions. *J. Phys. Soc. Jpn.* **1954**, *9* (5), 753–766.
- (62) Tanabe, Y.; Sugano, S. On the Absorption Spectra of Complex Ions II. *J. Phys. Soc. Jpn.* **1954**, *9* (5), 766–779.
- (63) Tanabe, Y.; Sugano, S. On the Absorption Spectra of Complex Ions, III The Calculation of the Crystalline Field Strength. *J. Phys. Soc. Jpn.* **1956**, *11* (8), 864–877.
- (64) Figgis, B. N.; Lewis, J. The Magnetic Properties of Polynuclear Transition Metal Complexes. *Progress in Inorganic Chemistry*; Cotton, E. A., Ed.; Interscience Publishers: New York, 1964; Vol. 6, p 37.
- (65) Lovesey, S. W. Magnetic Excitations in FeCl_2 . *J. Phys. C: Solid State Phys.* **1974**, *7* (11), 2049–2059.
- (66) Hutchings, M. T. Neutron Scattering Investigation of Magnetic Excitations in CoCl_2 . *J. Phys. C: Solid State Phys.* **1973**, *6* (21), 3143–3155.
- (67) Johnston, D. C. Magnetic Susceptibility of Collinear and Noncollinear Heisenberg Antiferromagnets. *Phys. Rev. Lett.* **2012**, *109* (7), No. 077201.
- (68) Johnston, D. C. Unified Molecular Field Theory for Collinear and Noncollinear Heisenberg Antiferromagnets. *Phys. Rev. B: Condens. Matter Mater. Phys.* **2015**, *91* (6), No. 064427.
- (69) Onsager, L. Crystal Statistics. I. A Two-Dimensional Model with an Order-Disorder Transition. *Phys. Rev.* **1944**, *65* (3–4), 117–149.
- (70) Cracknell, A. P.; Davies, B. L.; Miller, S. C.; Love, W. F. *Kronecker Product Tables*; IFI/Plenum: New York, 1979.
- (71) Gallego, S. V.; Tasci, E. S.; de la Flor, G.; Perez-Mato, J. M.; Aroyo, M. I. IUCr. Magnetic Symmetry in the Bilbao Crystallographic Server: A Computer Program to Provide Systematic Absences of Magnetic Neutron Diffraction. *J. Appl. Crystallogr.* **2012**, *45* (6), 1236–1247.
- (72) Fu-Tai Tuan, D.; Reed, J. W.; Hoffmann, R. Studies of the Linkage and Bonding of Triatomics in Transition Metal Complexes. Part 2. NCS^- Complexes. *J. Mol. Struct.: THEOCHEM* **1991**, *232* (C), 111–121.
- (73) Goodenough, J. B. An Interpretation of the Magnetic Properties of the Perovskite-Type Mixed Crystals $\text{La}_{1-x}\text{Sr}_x\text{CoO}_{3-x}$. *J. Phys. Chem. Solids* **1958**, *6*, 287–297.
- (74) Kanamori, J. Theory of the Magnetic Properties of Ferrous and Cobaltous Oxides. *Prog. Theor. Phys.* **1957**, *17* (2), 177–196.
- (75) Kanamori, J. Theory of the Magnetic Properties of Ferrous and Cobaltous Oxides. *Prog. Theor. Phys.* **1957**, *17* (2), 197–222.
- (76) DeFotis, G. C.; McGhee, E. M.; Echols, K. R.; Wiese, R. S. Magnetic and Structural Properties of $\text{Mn}(\text{SCN})_2(\text{ROH})_2$ Compounds. *J. Appl. Phys.* **1988**, *63* (8), 3569–3571.
- (77) DeFotis, G. C.; Wimberly, B. T.; Jeffers, R. B.; May, W. M.; Owens, T. M. Magnetic Behavior of Single-Crystal $\text{Co}(\text{SCN})_2(\text{CH}_3\text{OH})_2$: Three-Dimensional Ising Metamagnetism and Field-Induced Spin Reorientations. *Phys. Rev. B: Condens. Matter Mater. Phys.* **2007**, *76* (1), No. 014419.
- (78) Kmety, C. R.; Huang, Q.; Lynn, J. W.; Erwin, R. W.; Manson, J. L.; McCall, S.; Crow, J. E.; Stevenson, K. L.; Miller, J. S.; Epstein, A. J. Noncollinear Antiferromagnetic Structure of the Molecule-Based Magnet $\text{Mn}[\text{N}(\text{CN})_2]_2$. *Phys. Rev. B: Condens. Matter Mater. Phys.* **2000**, *62* (9), 5576–5588.
- (79) Huang, B.; Clark, G.; Navarro-Moratalla, E.; Klein, D. R.; Cheng, R.; Seyler, K. L.; Zhong, D.; Schmidgall, E.; McGuire, M. A.; Cobden, D. H.; Yao, W.; Xiao, D.; Jarillo-Herrero, P.; Xu, X. Layer-Dependent Ferromagnetism in a van Der Waals Crystal down to the Monolayer Limit. *Nature* **2017**, *546* (7657), 270–273.
- (80) Gong, C.; Li, L.; Li, Z.; Ji, H.; Stern, A.; Xia, Y.; Cao, T.; Bao, W.; Wang, C.; Wang, Y.; Qiu, Z. Q.; Cava, R. J.; Louie, S. G.; Xia, J.; Zhang, X. Discovery of Intrinsic Ferromagnetism in Two-Dimensional van Der Waals Crystals. *Nature* **2017**, *546* (7657), 265–269.
- (81) López-Cabrelles, J.; Mañas-Valero, S.; Vitorica-Yrezabal, I. J.; Bereciartua, P. J.; Rodríguez-Velamazán, J. A.; Waerenborgh, J. C.; Vieira, B. J. C.; Davidovikj, D.; Steeneken, P. G.; van der Zant, H. S. J.; Mínguez Espallargas, G.; Coronado, E. Isorecticular Two-Dimensional Magnetic Coordination Polymers Prepared through Pre-Synthetic Ligand Functionalization. *Nat. Chem.* **2018**, *10* (10), 1001–1007.
- (82) Hornick, C.; Rabu, P.; Drillon, M. Hybrid Organic–Inorganic Multilayer Materials: Influence of π Electrons as Magnetic Media in a Series of Bridged-Layer Compounds $\text{M}_2(\text{OH})_{4-x}\text{A}_{x/2}$ ($\text{M} = \text{Cu}(\text{II})$ or $\text{Co}(\text{II})$, $\text{A} = \text{dicarboxylate Anion}$). *Polyhedron* **2000**, *19* (3), 259–266.
- (83) Rabu, P.; Drillon, M.; Awaga, K.; Fujita, W.; Sekine, T. Hybrid Organic-Inorganic Multilayer Compounds: Towards Controllable and/or Switchable Magnets. In *Magnetism: Molecules to Materials*; Wiley-VCH Verlag GmbH & Co. KGaA: Weinheim, Germany, 2003; pp 357–395.